Robust maintenance of cell surface tension in mitosis by RhoA-driven myosin II mechanoresponse

Jingjing Ding[1,2,*], Chao Wang[1,2,*], Qiaodong Wei[3], Shoukang Du[1,2], Xiaobo Gong[3], Ting Gang Chew[1,2,#]

Affiliations

[1]Department of Orthopedics of the Second Affiliated Hospital, Zhejiang University School of Medicine, Zhejiang University, Hangzhou 310058, China

[2]The Zhejiang University-University of Edinburgh Institute, Zhejiang University School of Medicine, Zhejiang University, Hangzhou 310058, China

[3]Department of Engineering Mechanics, School of Naval Architecture, Ocean and Civil Engineering, Shanghai Jiao Tong University, Shanghai 200240, China

*Co-first authors

#Correspondence to: Ting Gang Chew (tinggchew@intl.zju.edu.cn)

Running title: Mechanoresponsive RhoA regulates NMII in mitosis

Abstract

As cells enter mitosis, cell cortex contraction generates surface tension to establish a geometry feasible for division in a physically confined environment. Cell surface tension rises in prophase and continues to stay constant during metaphase to support mitosis. How the cell surface tension is maintained throughout mitosis is not well explored. We show that the cell surface tension is actively maintained by a mechanosensitive RhoA pathway at the cell cortex during mitosis. Mechanical activation of RhoA leads to non-muscle myosin IIB (NMIIB) stabilization and mechanosensitive accumulation at the cell cortex via Rho kinase (ROCK) regulation of the NMIIB head domain. Interestingly, when the NMIIB tail domain regulation is perturbed, the NMIIB has reduced ability to generate tension but could still support mitotic cells to withstand compressive stress by undergoing mechanosensitive accumulation at the cell cortex. Thus, mechanical RhoA activation drives NMIIB mechanoresponse via its head domain regulation to maintain cell surface tension during mitosis.

Introduction

Most animal cells undergo a dramatic change of cell geometry when they enter mitosis (Ramkumar and Baum, 2016). Upon entry into mitosis, cells increase their intracellular hydrostatic pressure by water influx, and concomitantly, contracts the cell cortex to generate higher cell surface tension to counteract the hydrostatic force (Chugh et al., 2017; Ramanathan et al., 2015; Roubinet et al., 2012; Stewart et al., 2011). These cellular forces together lead to mitotic cell rounding that provides an ideal cell geometry to undergo mitosis and cytokinesis (Lancaster et al., 2013). Establishing and maintaining cell surface tension to sustain a minimum cell height for a functional cell geometry during mitosis is particularly important when cells are dividing in a physically confined tissue environment (Cattin et al., 2015; Matthews et al., 2020). Within a tissue environment, cells constantly experience mechanical stresses such as compressive stress from surrounding cells and the extracellular matrix. This is particularly significant in an overgrowth tumor environment where the excessive cell proliferation, cell infiltration and matrix deposition results in an accumulation of solid stress or compressive stress inside the tumors (Nia et al., 2016; Nia et al., 2020). Cells that are not able to withstand the compressive stress during mitosis have defects in their mitotic spindle stability and

form multipolar spindles that lead to chromosome mis-segregation and aneuploidy (Lancaster et al., 2013; Matthews et al., 2020). Thus, the ability to generate and sustain cell surface tension in mitotic cells in a crowded environment is important in maintaining their genome integrity (Cadart et al., 2014; Taubenberger et al., 2020). How mechanistically cells maintain cell surface tension during mitosis in a confined environment remains unclear.

Cells progressively increase their surface tension from prophase and maintain a constant high level of the surface tension throughout mitosis with the actin cortex homeostatically maintained (Nishimura et al., 2019; Stewart et al., 2011). Cell surface tension is generated by contractile forces derived from an actomyosin-based cell cortex. In the cell cortex, actin filaments turn over to maintain a homeostatic network for the molecular motor non-muscle myosin II (NMII) to slide and generate forces (Chew et al., 2017; Chugh et al., 2017). As cells enter mitosis, a Rho guanine nucleotide exchange factor (RhoGEF) Ect2 activates RhoA, which in turn binds to the cell membrane and recruits its effectors such as anillin, formin and Rho-associated kinase (ROCK) to activate actomyosin contractility at the cell cortex (Maddox and Burridge, 2003; Matthews et al., 2012; Ramanathan et al., 2015). Interestingly, NMIIs display mechanoresponse by accumulating at the cell cortex in response to mechanical stress (Effler et al., 2006; Schiffhauer et al., 2016; Schiffhauer et al., 2019). In addition, a tension-dependent activation of RhoA signaling has been detected at the cell-cell adherens junctions and the cell matrix focal adhesion to reinforce NMII contraction (Acharya et al., 2018; Guilluy et al., 2011). A similar mechanosensitive RhoA activation has not been demonstrated in mitosis to regulate NMII's mechanoresponse despite ROCK is required for NMII's mechanoresponse at the cell cortex (Schiffhauer et al., 2016).

Results and discussion

To study how cell surface tension is maintained during mitosis, we made a human MCF10A mammary epithelial cell stably expressing fluorescently tagged non-muscle myosin IIB (mEmerald-NMIIB) and active RhoA biosensor consisting of the RhoA-binding domain of anillin (mRuby2-AHPH)

(Budnar et al., 2019; Piekny and Glotzer, 2008). NMIIB localizes to the cell cortex in the early mitosis and functions downstream of active RhoA to generate cortical tension (Taneja et al., 2020). Live-cell microscopy imaging revealed that NMIIB and active RhoA localized to the cell cortex starting from early mitosis and enriched at the division site during mitosis and cytokinesis, consistent with previous studies and their roles in tension generation at the cell cortex during cell division (Fig. S1 A) (Piekny and Glotzer, 2008; Taneja et al., 2020). When mitotic cells were treated with a RhoA inhibitor C3 exoenzyme that prevents activation of RhoA, both active RhoA and NMIIB disappeared from the mitotic cell cortex (Fig. S1 B). This indicates that mRuby2-AHPH reliably reports the active state of RhoA, and NMIIB and anillin AHPH localizations report the status of cellular contractility during mitosis and cytokinesis.

We first addressed whether the maintenance of cortical NMIIB and cell surface tension during mitosis required an active NMIIB turnover. To this end, we treated mitotic cells with low, medium and high concentrations of the low cytotoxic and photostable NMII inhibitor *para*-nitro-blebbistatin (p-nitroblebb), which lowers the actin affinity of NMII heads (Kepiro et al., 2014; Rauscher et al., 2018). Mitotic cells treated with a low concentration of p-nitroblebb showed punctate cortical NMIIB patterns (Fig. 1 A, insets). Higher concentrations of p-nitroblebb resulted in a decreasing NMIIB intensity at the mitotic cell cortex (Figs. 1 A and B). Analyses of the NMIIB turnover at the mitotic cell cortex with the fluorescence recovery after photobleaching technique (FRAP) showed an increase of the immobile fractions of NMIIB upon increased concentrations of p-nitroblebb (Figs.1 C and D; DMSO: 0.27 ± 0.08; [Low]: 0.45 ± 0.01; [Medium]: 0.50 ± 0.01; [High]: 0.59 ± 0.03). The recovery half time of cortical NMIIB decreased when increasing concentrations of p-nitroblebb were used (Fig. 1 D; DMSO: 20.33 ± 2.09 s; [Low]: 12.61 ± 1.46 s; [Medium]: 11.30 ± 0.59 s; [High]: 9.49 ± 0.05 s). The FRAP analysis suggests that a decrease of NMIIB recovery half time with higher immobile fractions characterizes inhibition of NMIIB function at the cell cortex.

Next, we measured cell surface tension in mitotic cells treated with p-nitroblebb using the micropipette aspiration technique. The mitotic cell surface tension decreased to 56%, 44%, 31% of

101 the control group after treatments with low, medium and high concentrations of p-nitroblebb,
102 respectively (Fig. 1 E; DMSO: 894.90 ± 186.74 pN/μm; [Low]: 500.42 ± 90.64 pN/μm; [Medium]:
103 393.87 ± 121.08 pN/μm; [High]: 281.58 ± 60.84 pN/μm). Our data suggests that a low concentration
104 of p-nitroblebb reduced NMIIB capacity in tension generation despite having punctate localizations
105 at the cell cortex after treatment. This is similar to other contractile actomyosin machinery in which
106 the absence of NMII turnover results in NMII aggregation and low tension generation (Thiyagarajan
107 et al., 2021). Perturbation of NMII turnover by p-nitroblebb did not affect the actin cortex significantly
108 as its functional thickness remained largely similar after treatment (Fig. 1 F). Taken together, we
109 showed that an active NMII turnover at the cell cortex is required to maintain a contractile actomyosin
110 architecture and cell surface tension during mitosis.

111

112 Interestingly, we found that there was a decrease of the cortical localization of active RhoA when
113 cell surface tension has decreased for 3-fold in mitotic cells treated with a high concentration of p-
114 nitroblebb, suggesting that RhoA could respond to the cortical tension generated by NMII during
115 mitosis (Fig. 1 G). This contrasts with the upstream function of active RhoA in regulating NMII and
116 implies a mechanosensitive activation of RhoA during mitosis. To test whether RhoA and NMIIB
117 could be mechanically regulated, we compressed the mitotic cells with a soft elastic gel and a weight
118 (Fig. 2 A). When compressive forces were exerted on the mitotic cells, the cell has enlarged its
119 diameter, and the cell height has decreased from 22.89 ± 1.88 μm to 15.19 ± 1.19 μm (Figs. 2 B and
120 C). Within 2 minutes after compression, we observed increased intensity of active RhoA at the mitotic
121 cell cortex. In average, there was 1.54 ± 0.31-fold increase of cortical active RhoA intensity in
122 individual cells (Fig. 2 D). Concomitantly, NMIIB increased its intensity at the mitotic cell cortex by
123 1.45 ± 0.29-fold compared to that of before compression (Figs. 2 E and F). Approximately 76.5%
124 individual cells showed an increase of both active RhoA and NMIIB at the mitotic cell cortex after
125 compression (Fig. S2), suggesting that compressive forces exerted on the mitotic cell cortex activate
126 RhoA, which in turn activates NMIIB to generate higher cell surface tension to withstand the
127 mechanical stress. Consistently, we found that compression in mitotic cells has slowed down the
128 turnover of the cortical NMIIB, with an increase of the recovery half time of 27.75 ± 0.86 s as

129 compared to that of in the uncompressed mitotic cells that was 18.85 ± 1.79 s (Figs. 2 G and H).
130 Thus, compressive forces stabilize NMIIB at the mitotic cell cortex leading to a mechanosensitive
131 accumulation of NMIIB. Taken together, our results showed that active RhoA and NMIIB
132 demonstrate a mechanosensitive accumulation at the cell cortex to generate cell surface tension to
133 withstand compressive forces during mitosis.

134

135 We next studied how NMII's functions in cell surface tension generation and mechanoresponse are
136 regulated and interrelated during mitosis. NMII is regulated by the phosphorylation of its regulatory
137 light chain (RLC) that associates with the head domain and by the phosphorylation of the tail domain.
138 Phosphorylation of RLC at the NMII head domain increases NMII actin-activated ATPase activity
139 and promotes the formation of an unfolded active NMII to slide on actin filaments. Phosphorylation
140 of the tail domain is involved in regulating myosin II filament assembly (Heissler and Sellers, 2016).
141 We examined the contribution of NMII head and tail domain phosphoregulations on the tension
142 generation and the mechanoresponse of NMII during mitosis. Phosphorylation of RLC at the NMII
143 head domain is driven by a RhoA / ROCK signaling pathway (Fig. 3 A) (Amano et al., 1996). When
144 mitotic cells were chemically inhibited by the ROCK inhibitor Y-27632, NMIIB decreased for about
145 2-fold at the cell cortex while active RhoA did not show significant changes (Figs. 3 A and B).
146 Consistently, there was about 20% decrease of cell surface tension from 965.34 ± 133.34 pN/μm in
147 the control group to 770.04 ± 160.08 pN/μm in the Y-27632 treated group (Fig. 3 C). Of note, a
148 decrease of cell surface tension by the concentration of Y-27632 used in this study was not sufficient
149 to reduce active RhoA from the cell cortex.

150

151 When mitotic cells were compressed for about 8 minutes in the presence of Y-27632, there was a
152 decrease of cortical NMIIB as compared to the control group that showed an increase of cortical
153 NMIIB after compression (Figs. 3 D, E and F). Active RhoA showed a mechanosensitive
154 accumulation at the mitotic cell cortex after compression in the presence and absence of Y-27632
155 (Figs. 3 D and E and F). Importantly, the lack of NMIIB mechanosensitive accumulation at the mitotic

156 cell cortex after compression has further decreased the cell height after compression (Fig. 3 G; 13.62
157 ± 0.83 μm in DMSO treated compressed group and 11.08 ± 1.22 μm in Y-27632 treated compressed
158 group), which is a readout of how much the cells could resist the compressive stress. Thus, mitotic
159 cells were not able to generate sufficient cell surface tension to withstand the compressive force
160 when RhoA / ROCK pathway was defective. Collectively, our results showed that inhibition of the
161 RLC phosphorylation by ROCK has reduced NMII capacity in tension generation and in
162 mechanoresponse. Thus, NMII head domain phosphoregulation by RhoA / ROCK signaling is
163 required for both tension generation and mechanoresponse of NMII.

164

165 We next tested the role of NMIIB tail domain phosphorylation in regulating cell surface tension and
166 NMIIB mechanoresponse during mitosis. Phosphorylation of NMIIB S1935 lowers the ability of NMIIB
167 to assemble into myofilaments (Fig. 4 A) (Juanes-Garcia et al., 2015; Schiffhauer et al., 2019). We
168 first generated three cell lines stably expressing wild type NMIIB, NMIIB containing a non-
169 phosphorylatable alanine residue at S1935 (S1935A), and NMIIB containing a phosphomimetic
170 aspartate residue at S1935 (S1935D), respectively. The endogenous NMIIB in these cell lines was
171 depleted using CRISPR interference (CRISPRi) that switches off gene expression from its promoter
172 and does not interfere with the transgene expression (Fig. S3 A and B). Cells expressing NMIIB
173 S1935D showed a decrease in the cytoskeletal fraction compared to cells expressing wild type
174 NMIIB or NMIIB S1935A, indicating less NMIIB myofilaments were assembled (Fig. 4 B and C).

175

176 Next, we examined the mitotic cell surface tension and the NMIIB mechanoresponse in cells
177 expressing NMIIB tail phosphomutants. Interestingly, mitotic cells expressing NMIIB S1935D
178 generated lower cell surface tension (1007.94 ± 130.21 pN/μm in wild type NMIIB and 677.67 ±
179 111.03 pN/μm in NMIIB S1935D) but were able to demonstrate mechanosensitive accumulation of
180 NMIIB S1935D after compression (Figs. 4 D and E). Mitotic cells expressing NMIIB S1935A exhibited
181 a slightly higher level of cell surface tension (1069.76 ± 158.13 pN/μm in NMIIB S1935A) and
182 displayed a similar mechanoresponse as in cells expressing wild type NMIIB (Figs. 4 D and E). Thus,

183 phosphorylation of NMIIB S1935 at the tail domain affected NMIIB's function in cell surface tension
184 generation but less on the mechanoresponse of NMIIB, in line with the previous study showing that
185 the NMIIB tail domain fine-tuned the NMIIB mechanosensitive dynamics and the phosphomutants
186 could accumulate with varying degree at the cell cortex in epithelial cells in response to mechanical
187 stress (Schiffhauer et al., 2019). Importantly, the NMIIB S1935D generated sufficient mitotic cell
188 surface tension to withstand the compressive force exerted on the cells as evidenced by the similar
189 cell heights as in the cells expressing wild type NMIIB after compression (Fig. 4 F). Thus, the
190 mechanosensitive accumulation of NMIIB compensates for the decreased ability to generate tension
191 of the NMIIB phosphomimetic tail mutant. By accumulating more NMIIB at the cell cortex has allowed
192 cells to generate sufficient cell surface tension during mitosis under compression.

193

194 Our study revealed that during mitosis, cell surface tension is maintained by a mechanosensitive
195 RhoA / ROCK pathway that leads to the NMIIB accumulation at the cell cortex in a mechanically
196 constrained environment. Mechanosensitive accumulation of NMIIB is a result of a slowdown of
197 NMIIB turnover at the cell cortex, which we showed is important in maintaining a contractile
198 actomyosin architecture that sustains the mitotic cell surface tension. We further show that tension
199 generation and mechanoresponse are two mechanoproperties of NMIIB that can be uncoupled. The
200 phosphoregulation by RhoA / ROCK pathway at the NMII head domain is involved in both
201 mechanoproperties, whereas the phosphoregulation at the NMII tail domain is required mainly for
202 the tension generation and for fine-tuning the mechanoresponse of NMIIB.

203

204 Mechanical activation of RhoA happens at the cell-cell adherens junctions and the cell-matrix focal
205 adhesion to reinforce actomyosin contractility in response to mechanical stress (Acharya et al., 2018;
206 Guilluy et al., 2011). This study, to our knowledge, is first to show mechanoactivation of RhoA at the
207 cell cortex to sustain cell surface tension during mitosis. Mechanosensitve accumulation of active
208 RhoA at the cell cortex during mitosis was not previously identified although inhibition of its
209 downstream ROCK led to a decreased mechanoresponse of NMII (Schiffhauer et al., 2016). In this
210 study, we used a widely used live-cell active RhoA biosensor (Koh et al., 2021) and focused only on

211 mitotic cells using a microscopy with confocality and high temporal resolution. This has facilitated
212 the detection of a tension-dependent activation of RhoA at the cell cortex when mitosis is
213 mechanically challenged.

214

215 We showed that NMIIB's function in tension generation and its mechanoresponse can be uncoupled
216 by a phosphomimetic point mutation at S1935 of the tail domain, which perturbs assembly of NMIIB
217 myofilaments. This perturbation lowers NMIIB's ability to generate cell surface tension but does not
218 decrease NMIIB's ability to accumulate at the cell cortex in response to mechanical stress. The
219 functional uncoupling enables cells to withstand the mechanical stress by compensating with more
220 NMIIs at the cell cortex even the NMII is weaker in tension generation, enabling robust maintenance
221 of cell surface tension during mitosis.

222

223 NMII shows a decrease of ADP-release kinetics when experiencing opposing loads (Kovacs et al.,
224 2007). This increases the lifetime of actin-bound state of NMII and hence its duty ratio, which could
225 lead to the mechanoaccumulation of NMII upon compression (Luo et al., 2013). This is in line with
226 our FRAP analysis that NMIIB stabilizes at the cell cortex when cells experience compressive forces.
227 We propose that mechanosensitive activation of RhoA / ROCK signaling pathway leads to RLC
228 phosphorylation, which associates with an increase of the ATPase kinetics of myosin head domain
229 to increase the flux of ATP hydrolysis into ADP (Amano et al., 1996). This together with the load-
230 dependent decrease of ADP-release kinetics of NMII collectively increase the ADP-bound NMII that
231 has a higher actin-binding lifetime, leading to its accumulation at the cell cortex in response to
232 mechanical stress to maintain cell surface tension during mitosis.

233

234

235

236

237 **Materials and methods**

238 **Cell lines and culture**

239 MCF10A cell lines were cultured in DMEM F-12 (Shanghai BasalMedia) with Glutamax (Gibco), 5%
240 horse serum (Biological Industries), 20 ng/ml EGF (Gibco), 0.5 mg/ml Hydrocortisone
241 (MedChemExpress), 100 ng/ml Cholera toxin (Sigma), 10 μg/ml Insulin (Biological Industries), 1%
242 Pen/Strep (Biological Industries) at 37°C with 5% CO2. The MCF10A cell line was a gift from Dr.
243 Kuan Yoow Chan from Zhejiang University. The cells were authenticated by Sangon Biotech and
244 were routinely checked for mycoplasma contamination in the lab using Myco-Blue Mycoplasma
245 Detector (Vazyme). MCF10A cells expressing mRuby2-AHPH and mEmerald-NMIIB were prepared
246 by lentivirus transduction and were enriched using the fluorescence-activated cell sorting (FACS).
247 MCF10A cells expressing mEmerald-NMIIB WT, mEmerald-NMIIB S1935A, and mEmerald-NMIIB
248 S1935D, respectively, were prepared by lentivirus transduction and selected with 2 μg/ml puromycin
249 (Sangon Biotech) and were enriched using the FACS. To knockdown the endogenous NMIIB, the
250 lentivirus expressing pCRISPRi0003 containing the guiding RNA (gRNA) targeting the NMIIB's 5'
251 UTR region was transduced into the cells expressing NMIIB phosphomutants. Cells were selected
252 with 6 μg/ml blasticidin (Solarbio) for 6 days and were continued to grow without the antibiotic for
253 another 1 to 3 days before the experiments.

254 **Drug treatments**

255 The following drugs were used in the study: NMII inhibitor: p-nitro-blebbistatin (Cayman Chemical,
256 24171); Rho inhibitor: C3 exoenzyme (Cytoskeleton, CT04); ROCK inhibitor: Y-27632
257 (MedChemExpress, HY-10583); CDK1 inhibitor: RO-3306 (Selleckchem, S7747). DMSO was used
258 to dissolve p-nitro-blebbistatin, Y-27632, RO-3306. C3 exoenzyme was dissolved in water. Details
259 of concentrations used in the study are described in figure legends.

260 **Lentiviral expression constructs**

261 The following lentiviral transfer plasmids were used in the study: pTGL0427 containing mRuby2-
262 AHPH in which AHPH was subcloned from an Addgene plasmid #68026 (a gift from Michael Glozter)
263 and fused with mRuby2; pTGL0193 containing mEmerald-NMIIB, which was subcloned from an

264 Addgene plasmid #54192 (a gift from Michael Davidson); pTGL0373 containing mEmerald-NMIIB
265 S1935A; pTGL0374 containing mEmerald-NMIIB S1935D; pTGL0386 containing KRAB and dCas9
266 for CRISPRi (a gift from Jorge Ferrer, Addgene plasmid #118154); pCRISPRi0001 containing gRNA
267 5' GTGCTAAAGGAGCCCGGCGG 3' cloned into pTGL0386; pCRISPRi0002 containing gRNA 5'
268 GCTGGATCTGTGGTCGCGGC 3' cloned into pTGL0386; pCRISPRi0003 containing gRNA 5'
269 GGACTGAGGCGCTGGATCTG 3' cloned into pTGL0386. The 3rd generation lentiviral packaging
270 system was used to prepare lentiviral particles. In brief, packaging plasmids pRSV-Rev,
271 pMDLg/pRRE, pMD2.G (gifts from Didier Trono) were chemically transfected with the transfer
272 plasmid into the 293Ta packaging cell line (Genecopoeia, LT008) using GeneTwin transfection
273 reagent (Biomed, TG101). After 3 days, the culture medium was collected, filtered through a 0.45
274 μm filter, and then concentrated using the lentivirus concentration solution (Genomeditech, GM-
275 040801) before adding to MCF10A cells.

276 **Mitotic cell preparation**

277 To increase the mitotic cell number, cells cultured on the imaging chambered coverglass were
278 treated with 7.5 μM RO-3306 (Selleckchem) for 16 to 18 hours at 37 °C and were washed with the
279 pre-warmed culture medium for 3 times to release cells into mitosis and added with 1 ml of fresh
280 medium. Experiments were performed 40 minutes after the drug wash-off.

281 **Elastic polyacrylamide gel preparation**

282 The polyacrylamide gel used for cell compression was prepared as described in Matthews *et al*. and
283 Le Berre *et al*. with modifications (Le Berre et al., 2014; Matthews et al., 2020). Briefly, 18 mm glass
284 coverslips (Sangon, F518211) were treated with 10 μl Binding-silane (Sangon, C500226) for 10
285 minutes and then were rinsed with 100% ethanol and air-dried. To prepare soft elastic gels (2 kPa),
286 1 ml polyacrylamide gel solution was prepared by mixing 125 μl 40% w/v acrylamide (Sangon), 35
287 μl 2% bis-arcylamide (Sangon), 10 μl APS (10% in water, Sangon), and 830 μl water. After adding
288 and mixing 1 μl TEMED (Sangon) into the gel solution, about 350 μl of the final gel solution was
289 immediately transferred onto a flat glass slide and covered by the coverslip pre-treated with the
290 Binding-silane. After polymerization for 20 minutes, the gel and the attached coverslip were gently

291 removed from the glass slide using a surgical blade and were soaked in PBS for at least 2 hours and
292 followed by the incubation in cell culture media for overnight. In experiments that involved drug
293 treatment, the gels were incubated in media containing the drugs for overnight.

294 **Micropipette aspiration (MPA)**

295 The micropipette was prepared by first pulling a borosilicate glass capillary (Sutter Instrument, B100-
296 58-10) using the P-97 Micropipette puller (Sutter Instrument). Then, the thin end of a borosilicate
297 glass capillary was cut by a Microforge (Narishige) to a diameter of about 5.5 μm. The micropipette
298 was bent to a desired degree by heating it over an alcohol lamp and was filled with phosphate-
299 buffered saline (PBS) using the MicroFil (World Precision Instruments, MF34G-5). The micropipette
300 was installed to a micropipette holder, which was connected to a syringe pump (Harvard apparatus)
301 and a 25 ml serological plastic pipettes via a three-way valve. The micropipette was positioned under
302 an inverted microscope (Olympus, IX73) equipped with Olympus 60x objective lens (N.A. 1.35, U
303 Plan super apochromat), a micromanipulator system (Eppendorf, TransferMan 4r), and a CMOS
304 high speed camera (Vision Research, Phantom 410L, 333.33 nm / pixel).

305 To perform micropipette aspiration, cells were cultured on a one-well chambered coverglass (Cellvis,
306 C1-1.5H-N) for 24 hours and then were treated with 7.5 μM RO-3306 for 18 hours. Cells were
307 washed 3 times with fresh media and were added with fresh media containing 20 mM HEPES. Cells
308 were incubated for another 40 minutes to reach mitosis. When a mitotic cell was aspirated by the
309 micropipette, the microscopy image was captured and analyzed using Fiji to obtain the pipette radius
310 (R_p) and the cell radius (R_c). The cell length of about half a diameter of the pipette opening was
311 aspirated in. The water pressure changes (ΔP) as displayed on the 25 ml serological plastic pipette
312 was also recorded. Cell surface tension (T) was then calculated based on the Laplace equation, $T =$
313 $\Delta P / 2 (1/R_p - 1/R_c)$.

314 **Spinning-disk confocal microscopy for live-cell imaging**

315 Spinning-disk confocal microscopy was equipped with a Nikon Eclipse Ti2-E inverted microscope,
316 Nikon 60x oil-immersion objective lens (N.A. 1.40, Plan Apochromat Lambda), a spinning-disk
317 system (Yokogawa Electric Corporation, CSU-W1), a Photometrics Prime 95B sCMOS camera, a

318 Piezo Z stage (Physik Instrumente), and a live-cell stage top chamber with humidified CO_2 (Okolab).
319 Images were acquired using the Metamorph with a z-step size of 0.5 μm and a x-y plane resolution
320 of 183.33 nm / pixel. The fluorophores were excited by laser lines at wavelengths of 488, 561, or 640
321 nm. For experiments involving cell compression, a z-stack of 30 μm was acquired before cells were
322 compressed and a stack of 22 μm was acquired after cells were compressed. This ensured that the
323 entire cell volume was covered during imaging. To quantitate the actin cortex thickness using the
324 super-resolution microscopy in Figure 1 F, images were acquired using the LiveSR super-resolution
325 module (Gataca) installed on the spinning-disk confocal microscope. For microscopy imaging not
326 involving cell compression, the μ-Slide 8-well chambered coverglass (ibidi, 80826) was used for cell
327 culture and imaging. Mitotic chromosomes were labeled with 0.2 μM SiR-DNA in live cells during
328 imaging (Cytoskeleton, CY-SC007).

329 **Mitotic cell compression and live-cell imaging**

330 To compress cells, 8 x 10^4 cells were first seeded on a 20 mm two-well chambered cover glass
331 (Cellvis, C2-1.5H-N). Forty-eight hours later, cells were treated with 7.5 μM RO-3306 to synchronize
332 cells at the G2/M boundary for 16 to 18 hours. Prior to live-cell imaging with compression,
333 synchronized cells were washed 3 times with the pre-warmed medium and added with 1 ml of fresh
334 medium and incubated in the stage-top chamber attached to the spinning-disk microscopy for 40
335 minutes. When compressing the mitotic cells, the coverslip coated with the elastic gel was put over
336 the cell layer and followed by a 5 g weight. Elastic gels and weights were pre-heated to 37 °C in the
337 chamber. In experiments where cells were treated with DMSO or 20 μM Y-27632, 1 ml medium
338 containing 40 μM Y-27632 or containing equivalent volume of DMSO was added to cells grown in 1
339 ml medium on the chambered coverglass to achieve a final concentration of 20 μM. The elastic gel
340 that was pre-incubated with 20 μM Y-27632 for overnight was then put on top of the cell layer and
341 followed by a 5 g weight. Cells at the same position were imaged before and after compression. The
342 cell compression efficiency was validated by their decrease of cell heights.

343

344

345 **Image analysis and processing**

346 Microscopy images were analyzed using Fiji. To quantitate fluorescence intensity of mEmerald-
347 NMIIB and mRuby2-AHPH in mitotic cells (Figs. 1 B, 1 G, S1 B, 3 A) and in mitotic cells for
348 compression experiments (Figs. 2 D, 2 F, 3 E, 3 F, 4 E), image stacks containing 5 slices around the
349 mid-plane were projected along the z-axis using the sum-intensity projection (Fiji/image/stacks/Z
350 project). Background subtraction (Fiji/process/subtract background) was performed on projected
351 images using the rolling ball radius of 20 pixels. Then, a segmented line with a line width of 4 (for
352 mitotic cells) or 5 (for mitotic cells in compression experiments) was used to select the cortical
353 fluorescent signals over the entire cell circumference. The mean fluorescence intensity of the
354 selected line region from the same cells before and after treatment and/or compression was
355 measured. The fold change was then calculated by dividing the intensity after treatment and/or
356 compression to the intensity before treatment and/or compression. For time series in Fig. 1 B, the
357 mean intensity of the cortical fluorescence was measured every 45 s. To quantitate the cell height
358 in cell compression experiments, the number of slices from top to bottom of a cell were multiplied by
359 0.5 μm. To quantitate the actin cortex thickness, a line was drawn across the cortical actin to obtain
360 a point spread function. The full-width-half-maximum of the point spread function was used to
361 indicate the thickness.

362 **FRAP**

363 FRAP was performed using the above-mentioned spinning-disk confocal microscopy equipped with
364 Nikon 100x oil-immersion objective lens (N.A. 1.45, Plan Apochromat Lambda) and iLAS2 FRAP
365 system (Gataca). Images were acquired using the Metamorph software at 110 nm / pixel. The
366 mEmerald-NMIIB fluorescence signal was photobleached by using a short pulse of high power 488
367 nm laser lines and imaged by using a low power 488 nm laser lines. A small bleaching rectangular
368 region-of-interest (ROI) of about 2 x 10-μm was drawn on the cortical mEmerald-NMIIB in mitotic
369 cells. Three frames of pre-bleached images were acquired with 1 second interval before
370 photobleaching, followed by time-lapse imaging of the same cells with 2 seconds interval for 120
371 seconds. The bleaching ROIs were recorded to locate the regions of bleaching during analysis.

372 Fiji was used to quantitate the fluorescence intensity of FRAP images. Background subtraction
373 (Fiji/process/subtract background) was performed on the images with the rolling ball radius of 20
374 pixels. A segmented line ROI (line width 5) was used to select the FRAP regions for quantification.
375 The mean intensity of ROIs for pre-bleached images and after bleached images ($I_{bleached}$) was
376 calculated for each time point. A mean pre-bleached intensity ($I_{prebleach}$) was derived from the average
377 of three pre-bleached images. The ratio of $I_{bleached}$ / $I_{prebleach}$ at each time point was calculated and
378 was subsequently deducted by the ratio of the first image after photobleaching to obtain $ratio_t$. The
379 $ratio_t$ of each time point was plotted as the recovery curve and fitted using a non-linear fitting function
380 (one-phase association function constrained by Y0 = 0 and plateau < 1) in the Prism 9 software
381 (GraphPad). The recovery time was derived from the half-time parameter calculated from the fitting.
382 The mobile fraction was derived from the span parameter calculated from the fitting. The immobile
383 fraction was calculated as a difference between 1 and the mobile fraction.

384 **Cytoskeletal fractionation and immunoblotting**

385 Cells were washed once with ice-cold PBS. To a single well of a 6-well cell culture plate, 200 μl of
386 lysis buffer (50 mM PIPES, pH 6.8, 46 mM NaCl, 2.5 mM EGTA, 1 mM $MgCl_2$, 0.5% Triton-X 100,
387 protease inhibitor cocktail) was added. Lysates were harvested and centrifuged at 13000 *g* for 20
388 minutes at 4°C. The supernatant (soluble fraction) was separated from the pellet (cytoskeletal
389 fraction). The pellet was then resuspended in a same volume of lysis buffer as the supernatant. Both
390 fractions were added with 5 x Laemli sample buffer and boiled for 5 minutes. The pellet suspension
391 was sonicated in a water bath sonicator for 1 minute with 20% power to improve solubility. Protein
392 samples were separated in a pre-cast SDS-PAGE gel (GenScript, M00657) and blotted to a PVDF
393 membrane (EMD Millipore, immobilon-P, IPVH00010). Blots were blocked with 5% skim milk for 1
394 hour at room temperature and were incubated at 4°C overnight with the NMIIB antibody (Proteintech,
395 19673-1-AP) or the β-actin antibody (HuaBio, ET1701-80). The secondary antibody used was Alexa
396 Fluor Plus 800-conjugated goat anti-rabbit IgG secondary antibody (ThermoFisher, A32735). Blots
397 were imaged using the LI-COR Odyssey CLx imaging system. The signal intensity of protein bands
398 was calculated using the LI-COR Image Studio software. The cytoskeletal fraction was calculated
399 by dividing the cytoskeletal fraction intensity by the sum intensity of cytoskeletal and soluble fractions.

400 Measurements in Fig. 4 C were obtained from four proteins blots derived from four independent
401 experiments. For the blot in Fig. S 3 A, primary antibodies used were NMIIB antibody (Proteintech,
402 19673-1-AP) and GAPDH antibody (Cell Signaling Technology, #5174). The secondary antibody
403 used was Alexa Fluor Plus 800-conjugated goat anti-rabbit IgG secondary antibody (ThermoFisher,
404 A32735).

405 **Quantitative real-time PCR (qPCR) for checking endogenous NMIIB**

406 To validate the knockdown of endogenous NMIIB in cells expressing the phosphomutants used in
407 Figure 4 E and 4 F, total RNAs were prepared from cells using the FastPure Cell/Tissue Total RNA
408 Isolation Kit (Vazyme, RC101-01) and were reverse transcribed into cDNA using the HiScript II Q
409 RT SuperMix for qPCR (Vazyme, R223-01). The expression level of cDNAs was determined using
410 the real-time PCR with the ChamQ Universal SYBR qPCR Master Mix (Vazyme, Q711-02). The
411 reaction mix was assembled on the hard-shell PCR plate (Bio-Rad, HSP9655), sealed with the
412 Microseal 'B' seal (Bio-Rad, MSB1001), and was performed in the CFX96 Touch Real-Time PCR
413 Detection System (Bio-RAD, C1000). Primers used in the qPCR: GAPDH, 5'
414 CAGGAGGCATTGCTGATGAT 3' and 5' GAAGGCTGGGGCTCATTT 3'; NMIIB, 5'
415 CCTCATGCTGACCTTGCAAA 3' and 5' GGACACAAAACCAATATTCCCATT 3'. The primer pair for
416 NMIIB targets the 3' UTR of NMIIB gene, allowing checking of endogenous NMIIB expression. The
417 C_T value for GAPDH was used for normalization to obtain the relative expression level.

418 **Statistical analysis**

419 Statistical analysis was performed using Prism 9 (GraphPad). Datasets were analyzed by Student t-
420 test. If datasets were not normally distributed, they were analyzed using the Mann-Whitney test. All
421 graphs were plotted using Prism 9 (GraphPad).

422

423 **Author contributions**

424 J.D. and C.W. designed, performed experiments, and analyzed data. S.D. prepared elastic gels used
425 in the study. Q.W and X.G provided the devices and technical expertise for micropipette aspiration.

426 T.G.C conceived the study, designed experiments, supervised the study, and prepared the
427 manuscript with inputs from all authors.

428

429 **Acknowledgement**

430 This study was funded by the Zhejiang University International Campus start-up grant (130000-
431 541902/016) given to T.G.C. We thank Dr. Di Chen for sharing the CRISPRi vector with us. We thank
432 Dr. Mikael Bjorklund for sharing the 293Ta packaging cell line with us. We thank Dr. Wanzhong Ge
433 and Dr. Junqi Huang for their comments on the manuscript. Special thanks to Dr. Fang Kong from
434 the Nanyang Technological University, Singapore for designing the imaging chamber adaptor used
435 in the microscopy imaging for cell compression. Q.W and X.G would like to acknowledge the support
436 from the National Natural Science Foundation of China (12072198).

437

438 **Competing interests**

439 The authors declare no competing interests.

440 **References**

441

442 Acharya, B.R., A. Nestor-Bergmann, X. Liang, S. Gupta, K. Duszyc, E. Gauquelin, G.A. Gomez, S.
443 Budnar, P. Marcq, O.E. Jensen, Z. Bryant, and A.S. Yap. 2018. A Mechanosensitive RhoA
444 Pathway that Protects Epithelia against Acute Tensile Stress. *Dev Cell*. 47:439-452 e436.
445 Amano, M., M. Ito, K. Kimura, Y. Fukata, K. Chihara, T. Nakano, Y. Matsuura, and K. Kaibuchi. 1996.
446 Phosphorylation and activation of myosin by Rho-associated kinase (Rho-kinase). *J Biol*
447 *Chem*. 271:20246-20249.
448 Budnar, S., K.B. Husain, G.A. Gomez, M. Naghibosadat, A. Varma, S. Verma, N.A. Hamilton, R.G.
449 Morris, and A.S. Yap. 2019. Anillin Promotes Cell Contractility by Cyclic Resetting of RhoA
450 Residence Kinetics. *Dev Cell*. 49:894-906 e812.
451 Cadart, C., E. Zlotek-Zlotkiewicz, M. Le Berre, M. Piel, and H.K. Matthews. 2014. Exploring the
452 function of cell shape and size during mitosis. *Dev Cell*. 29:159-169.
453 Cattin, C.J., M. Duggelin, D. Martinez-Martin, C. Gerber, D.J. Muller, and M.P. Stewart. 2015.
454 Mechanical control of mitotic progression in single animal cells. *Proc Natl Acad Sci U S A*.
455 112:11258-11263.
456 Chew, T.G., J. Huang, S. Palani, R. Sommese, A. Kamnev, T. Hatano, Y. Gu, S. Oliferenko, S.
457 Sivaramakrishnan, and M.K. Balasubramanian. 2017. Actin turnover maintains actin filament
458 homeostasis during cytokinetic ring contraction. *J Cell Biol*. 216:2657-2667.
459 Chugh, P., A.G. Clark, M.B. Smith, D.A.D. Cassani, K. Dierkes, A. Ragab, P.P. Roux, G. Charras,
460 G. Salbreux, and E.K. Paluch. 2017. Actin cortex architecture regulates cell surface tension.
461 *Nat Cell Biol*. 19:689-697.
462 Effler, J.C., Y.S. Kee, J.M. Berk, M.N. Tran, P.A. Iglesias, and D.N. Robinson. 2006. Mitosis-specific
463 mechanosensing and contractile-protein redistribution control cell shape. *Curr Biol*. 16:1962-
464 1967.
465 Guilluy, C., V. Swaminathan, R. Garcia-Mata, E.T. O'Brien, R. Superfine, and K. Burridge. 2011. The
466 Rho GEFs LARG and GEF-H1 regulate the mechanical response to force on integrins. *Nat*
467 *Cell Biol*. 13:722-727.
468 Heissler, S.M., and J.R. Sellers. 2016. Various Themes of Myosin Regulation. *J Mol Biol*. 428:1927-
469 1946.
470 Juanes-Garcia, A., J.R. Chapman, R. Aguilar-Cuenca, C. Delgado-Arevalo, J. Hodges, L.A.
471 Whitmore, J. Shabanowitz, D.F. Hunt, A.R. Horwitz, and M. Vicente-Manzanares. 2015. A
472 regulatory motif in nonmuscle myosin II-B regulates its role in migratory front-back polarity. *J*
473 *Cell Biol*. 209:23-32.
474 Kepiro, M., B.H. Varkuti, L. Vegner, G. Voros, G. Hegyi, M. Varga, and A. Malnasi-Csizmadia. 2014.
475 para-Nitroblebbistatin, the non-cytotoxic and photostable myosin II inhibitor. *Angew Chem Int*
476 *Ed Engl*. 53:8211-8215.
477 Koh, S.P., N.P. Pham, and A. Piekny. 2021. Seeing is believing: tools to study the role of Rho
478 GTPases during cytokinesis. *Small GTPases*:1-14.
479 Kovacs, M., K. Thirumurugan, P.J. Knight, and J.R. Sellers. 2007. Load-dependent mechanism of
480 nonmuscle myosin 2. *Proc Natl Acad Sci U S A*. 104:9994-9999.
481 Lancaster, O.M., M. Le Berre, A. Dimitracopoulos, D. Bonazzi, E. Zlotek-Zlotkiewicz, R. Picone, T.
482 Duke, M. Piel, and B. Baum. 2013. Mitotic rounding alters cell geometry to ensure efficient
483 bipolar spindle formation. *Dev Cell*. 25:270-283.
484 Le Berre, M., E. Zlotek-Zlotkiewicz, D. Bonazzi, F. Lautenschlaeger, and M. Piel. 2014. Methods for
485 two-dimensional cell confinement. *Methods Cell Biol*. 121:213-229.
486 Luo, T., K. Mohan, P.A. Iglesias, and D.N. Robinson. 2013. Molecular mechanisms of cellular
487 mechanosensing. *Nat Mater*. 12:1064-1071.
488 Maddox, A.S., and K. Burridge. 2003. RhoA is required for cortical retraction and rigidity during
489 mitotic cell rounding. *J Cell Biol*. 160:255-265.

490 Matthews, H.K., U. Delabre, J.L. Rohn, J. Guck, P. Kunda, and B. Baum. 2012. Changes in Ect2
491 localization couple actomyosin-dependent cell shape changes to mitotic progression. *Dev*
492 *Cell*. 23:371-383.
493 Matthews, H.K., S. Ganguli, K. Plak, A.V. Taubenberger, Z. Win, M. Williamson, M. Piel, J. Guck,
494 and B. Baum. 2020. Oncogenic Signaling Alters Cell Shape and Mechanics to Facilitate Cell
495 Division under Confinement. *Dev Cell*. 52:563-573 e563.
496 Nia, H.T., H. Liu, G. Seano, M. Datta, D. Jones, N. Rahbari, J. Incio, V.P. Chauhan, K. Jung, J.D.
497 Martin, V. Askoxylakis, T.P. Padera, D. Fukumura, Y. Boucher, F.J. Hornicek, A.J.
498 Grodzinsky, J.W. Baish, L.L. Munn, and R.K. Jain. 2016. Solid stress and elastic energy as
499 measures of tumour mechanopathology. *Nat Biomed Eng*. 1.
500 Nia, H.T., L.L. Munn, and R.K. Jain. 2020. Physical traits of cancer. *Science*. 370.
501 Nishimura, K., Y. Johmura, K. Deguchi, Z. Jiang, K.S.K. Uchida, N. Suzuki, M. Shimada, Y. Chiba,
502 T. Hirota, S.H. Yoshimura, K. Kono, and M. Nakanishi. 2019. Cdk1-mediated DIAPH1
503 phosphorylation maintains metaphase cortical tension and inactivates the spindle assembly
504 checkpoint at anaphase. *Nat Commun*. 10:981.
505 Piekny, A.J., and M. Glotzer. 2008. Anillin is a scaffold protein that links RhoA, actin, and myosin
506 during cytokinesis. *Curr Biol*. 18:30-36.
507 Ramanathan, S.P., J. Helenius, M.P. Stewart, C.J. Cattin, A.A. Hyman, and D.J. Muller. 2015. Cdk1-
508 dependent mitotic enrichment of cortical myosin II promotes cell rounding against
509 confinement. *Nat Cell Biol*. 17:148-159.
510 Ramkumar, N., and B. Baum. 2016. Coupling changes in cell shape to chromosome segregation.
511 *Nat Rev Mol Cell Biol*. 17:511-521.
512 Rauscher, A.A., M. Gyimesi, M. Kovacs, and A. Malnasi-Csizmadia. 2018. Targeting Myosin by
513 Blebbistatin Derivatives: Optimization and Pharmacological Potential. *Trends Biochem Sci*.
514 43:700-713.
515 Roubinet, C., P.T. Tran, and M. Piel. 2012. Common mechanisms regulating cell cortex properties
516 during cell division and cell migration. *Cytoskeleton (Hoboken)*. 69:957-972.
517 Schiffhauer, E.S., T. Luo, K. Mohan, V. Srivastava, X. Qian, E.R. Griffis, P.A. Iglesias, and D.N.
518 Robinson. 2016. Mechanoaccumulative Elements of the Mammalian Actin Cytoskeleton.
519 *Curr Biol*. 26:1473-1479.
520 Schiffhauer, E.S., Y. Ren, V.A. Iglesias, P. Kothari, P.A. Iglesias, and D.N. Robinson. 2019. Myosin
521 IIB assembly state determines its mechanosensitive dynamics. *J Cell Biol*. 218:895-908.
522 Stewart, M.P., J. Helenius, Y. Toyoda, S.P. Ramanathan, D.J. Muller, and A.A. Hyman. 2011.
523 Hydrostatic pressure and the actomyosin cortex drive mitotic cell rounding. *Nature*. 469:226-
524 230.
525 Taneja, N., M.R. Bersi, S.M. Baillargeon, A.M. Fenix, J.A. Cooper, R. Ohi, V. Gama, W.D. Merryman,
526 and D.T. Burnette. 2020. Precise Tuning of Cortical Contractility Regulates Cell Shape during
527 Cytokinesis. *Cell Rep*. 31:107477.
528 Taubenberger, A.V., B. Baum, and H.K. Matthews. 2020. The Mechanics of Mitotic Cell Rounding.
529 *Front Cell Dev Biol*. 8:687.
530 Thiyagarajan, S., S. Wang, T.G. Chew, J. Huang, M.K. Balasubramanian, and B. O'Shaughnessy.
531 2021. Myosin turnover controls actomyosin contractile instability. *BioRxiv*.
532 10.1101/2021.03.18.436017.

533

534 **Figure legends**

535 **Figure 1.** Maintenance of the mitotic cell surface tension and the cortical active RhoA requires NMIIB
536 turnover. (A) Micrographs of the cortical mEmerald-NMIIB in mitotic cells treated with different
537 concentrations of p-nitroblebb. Cells before and 15 minutes after the treatments were shown. [Low]
538 is 37 μM; [Medium] is 74 μM; [High] is 110 μM. Insets show a zoom-in view of the punctate NMIIB.
539 (B) Relative changes of cortical NMIIB intensity as a function of time. The fluorescence intensity at
540 each time point was normalized to that of in cells before treatments. Dotted lines indicate standard
541 deviation. DMSO, 12 cells; low, 9 cells; medium, 9 cells; high, 10 cells. (C) Recovery curves of
542 mEmerald-NMIIB fluorescence intensity after photobleaching in cells treated with different
543 concentrations of p-nitroblebb. DMSO, 36 cells; low, 36 cells; medium, 30 cells; high, 28 cells. (D)
544 Quantification of the recovery time and the immobile fraction of mEmerald-NMIIB by FRAP. (E)
545 Measurement of the mitotic cell surface tension by MPA in the presence of different concentrations
546 of p-nitroblebb. The inset shows an example of an aspirated cell. DMSO, 33 cells; low, 40 cells;
547 medium, 39 cells; high, 43 cells. (F) Quantification of the actin cortex thickness in mitotic cells
548 expressing actin chromobody treated with different concentrations of p-nitroblebb. 40 cells in each
549 treatment were counted. (G) Relative changes of active RhoA intensity at the cell cortex after DMSO
550 or 110 μM p-nitroblebb treatments as a function of time. The fluorescence intensity at each time point
551 was normalized to that of in cells before treatments. DMSO, 11 cells; p-nitroblebb, 17 cells.
552 Representative cells showing the decrease of active RhoA at the mitotic cell cortex before and after
553 p-nitroblebb treatment are shown.

554 Data represent means ± SD, except for (C) where data represent ± SEM. Scale bar, 5 μm.

555 **Figure 2.** NMIIB and active RhoA display mechanosensitive accumulation at the cell cortex during
556 mitosis. (A) A schematic representation of the mitotic cell compression experiment. A soft elastic
557 polyacrylamide gel (2 kPa) was used in the study. (B) A representative cell before and after
558 compression is shown. XY, top view; XZ, side view. (C) Quantification of the cell height before and
559 after compression. 56 cells were counted for their cell height before and after compression. (D)
560 Intensity of active RhoA in mitotic cells before and after compression was quantitated. Black dots
561 indicate the intensity before compression and orange dots indicate the intensity after compression

562 of the same cells. A representative cell with increased cortical active RhoA after compression is
563 shown. 26 cells were counted. (E) Two representative cells with increased accumulation of NMIIB at
564 the cell cortex are shown. (F) Intensity of the cortical NMIIB in mitotic cells before and after
565 compression was quantitated. Black dots indicate the intensity before compression and orange dots
566 indicate the intensity after compression of the same cells. 21 cells were counted. (G) Recovery
567 curves of the cortical mEmerald-NMIIB intensity in uncompressed cells and in compressed cells after
568 photobleaching. Uncompressed, 55 cells; compressed, 48 cells. (H) Quantification of the recovery
569 time and the immobile fraction of mEmerald-NMIIB by FRAP.

570 Data represent means ± SD, except for (G) where data represent ± SEM. Scale bar, 5 μm.

571 **Figure 3.** Phosphoregulation of the myosin II head domain is required to maintain the mitotic cell
572 surface tension and the NMIIB mechanosensitive response. (A) A schematic representation of the
573 regulation of RLC phosphorylation by Rho / ROCK signaling pathway at the myosin II head domain
574 is shown. P indicates phosphorylation. The cortical NMIIB and active RhoA at the cell cortex of mitotic
575 cells before and after DMSO or 20 μM Y-27632 treatments are shown. (B) Quantification of the
576 changes of NMIIB and active RhoA intensities at the cell cortex before and after DMSO or 20 μM Y-
577 27632 treatments. The fold change is a ratio of the mean intensity after treatments to the mean
578 intensity before treatment. NMIIB (DMSO), 26 cells; NMIIB (Y-27632), 47 cells; active RhoA (DMSO),
579 30 cells; active RhoA (Y-27632), 55 cells. (C) Measurement of the mitotic cell surface tension by
580 MPA in cells treated with DMSO or 20 μM Y-27632. DMSO, 59 cells; Y-27632, 59 cells. (D) The
581 cortical NMIIB and active RhoA at the cell cortex of mitotic cells before and after DMSO or 20 μM Y-
582 27632 treatments with compression are shown. (E) Quantification of the changes of NMIIB and
583 active RhoA intensities at the cell cortex before and after treatments of DMSO or 20 μM Y-27632
584 with compression. The fold change is a ratio of the mean intensity after treatments and compression
585 to the mean intensity before treatment and compression. NMIIB (DMSO + compression), 25 cells;
586 NMIIB (Y-27632 + compression), 25 cells; active RhoA (DMSO + compression), 24 cells; active
587 RhoA (DMSO + compression), 21 cells. (F) Intensity changes for NMIIB and active RhoA at the cell
588 cortex in mitotic cells treated with DMSO or 20 μM Y-27632. Individual changes are shown. The fold
589 change in 3 E was calculated based on the individual fold change of the intensity in 3 F. (G)

590 Quantification of the cell height before and after treatment of DMSO or 20 μM Y-27632 with
591 compression. 25 cells in each treatment and compression were counted for their cell heights.

592 Data represent means ± SD. Scale bar, 5 μm.

593 **Figure 4.** Perturbation of the NMIIB tail domain regulation affects maintenance of the mitotic cell
594 surface tension but less on the NMIIB mechanoresponse. (A) A schematic representation of the
595 phosphoregulation of the NMIIB tail domain in controlling the myosin II filament assembly. (B)
596 Western blotting shows the cytoskeletal fractions and soluble fractions of NMIIB and actin in
597 MCF10A cells expressing different phosphomutants in the absence of endogenous NMIIB. KD,
598 knockdown. (C) Quantification of the cytoskeletal fractions of NMIIB wild type or phosphomutants
599 from the western blotting. (D) Measurement of the mitotic cell surface tension by MPA in cells
600 expressing NMIIB (WT), NMIIB (S1935A), or NMIIB (S1935D). NMIIB (WT), 59 cells; NMIIB
601 (S1935A), 40 cells; NMIIB(S1935D), 40 cells. (E) Quantification of the changes of NMIIB (WT),
602 NMIIB (S1935A), and NMIIB (S1935D) at the cell cortex before and after compression. The fold
603 change is a ratio of the mean intensity after compression to the mean intensity before compression.
604 The dotted indicates ratio of 1 in which a ratio higher than 1 means a positive mechanoresponse.
605 NMIIB (WT), 30 cells; NMIIB (S1935A), 28 cells; NMIIB (S1935D), 28 cells. (F) Quantification of the
606 cell height in cells expressing NMIIB (WT), NMIIB (S1935A), or NMIIB (S1935D) before and after
607 compression. NMIIB (WT), 30 cells; NMIIB (S1935A), 21 cells, NMIIB (S1935D), 26 cells.

608 Data represent means ± SD.

609 **Figure S1.** Establishment of a MCF10A cell line stably expressing mEmerald-NMIIB and mRuby2-
610 AHPH (active RhoA). (A) Micrographs of a representative cell showing mEmerald-NMIIB and active
611 RhoA localization during mitosis and cytokinesis. (B) Effect of C3 exoenzyme treatment on the
612 cortical NMIIB and active RhoA in a mitotic cell is shown. The changes of NMIIB and active RhoA
613 intensities at the mitotic cell cortex before and after 10 μg/ml C3 exoenyzme treatments were
614 quantified. The fold change is a ratio of the mean intensity after 10 μg/ml C3 exoenzyme treatment
615 to the mean intensity before treatment. The control group was added with media as C3 exoenzyme

616 was dissolved in water. NMIIB (control), 22 cells; NMIIB (C3 exoenzyme), 37 cells; active RhoA
617 (control), 35 cells; active RhoA (C3 exoenzyme), 36 cells.

618 Data represent means ± SD. Scale bar, 5 μm.

619 **Figure S2.** Increased accumulation of NMIIB and active RhoA at the mitotic cell cortex in the same
620 individual cells. Fold changes of NMIIB and active RhoA at the mitotic cell cortex after compression
621 in individual cells were plotted.

622 **Figure S3.** Identification of gRNA sequences that could knockdown NMIIB expression by CRISPRi.
623 (A) Western blotting shows the knockdown efficiency of endogenous NMIIB by CRISPRi using 3
624 different guiding RNAs (gRNAs). Highlighted gRNA 3 was used in the study to knock down NMIIB.
625 (B) Relative expression of endogenous NMIIB in MCF10A cells, MCF10A cells expressing wild type
626 NMIIB or phosphomutants as determined by qPCR.

627 Data represent means ± SD.

Figure 1

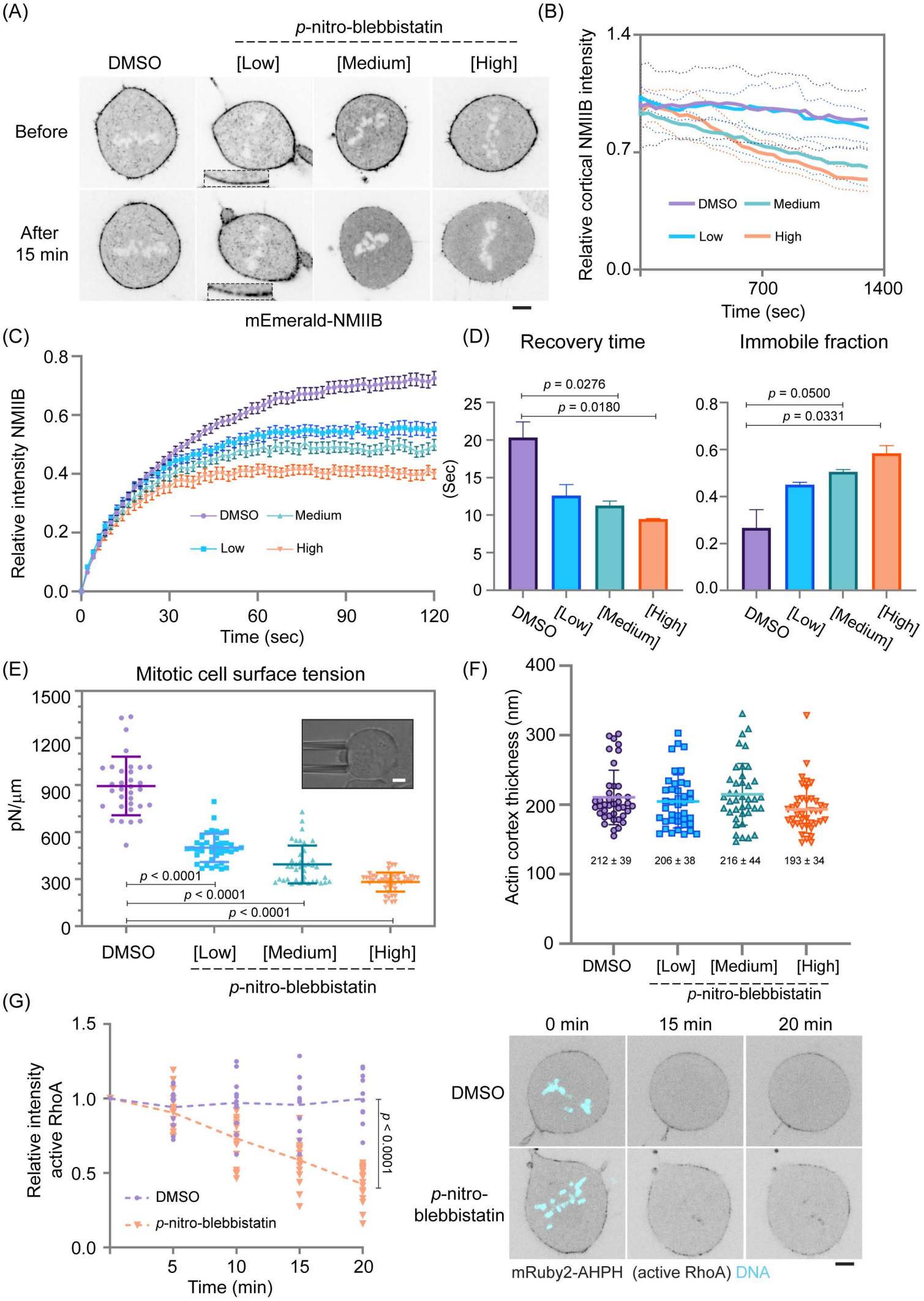
(A)
p-nitro-blebbistatin
DMSO
[Low]
[Medium]
[High]
Before
After 15 min
mEmerald-NMIIB
(B)
Relative cortical NMIIB intensity
1.4
0.7
0.0
700
1400
Time (sec)
DMSO
Medium
Low
High
(C)
Relative intensity NMIIB
0.8
0.6
0.4
0.2
0.0
0
30
60
90
120
Time (sec)
DMSO
Medium
Low
High
(D)
Recovery time
Immobile fraction
p = 0.0276
p = 0.0180
(Sec)
25
20
15
10
5
0
DMSO
[Low]
[Medium]
[High]
p = 0.0500
p = 0.0331
0.8
0.6
0.4
0.2
0.0
(E)
Mitotic cell surface tension
pN/μm
1500
1200
900
600
300
0
p < 0.0001
p < 0.0001
p < 0.0001
DMSO
[Low]
[Medium]
[High]
p-nitro-blebbistatin
(F)
Actin cortex thickness (nm)
400
300
200
100
0
212 ± 39
206 ± 38
216 ± 44
193 ± 34
DMSO
[Low]
[Medium]
[High]
p-nitro-blebbistatin
(G)
Relative intensity active RhoA
1.5
1.0
0.5
0.0
5
10
15
20
Time (min)
DMSO
p-nitro-blebbistatin
p < 0.0001
0 min
15 min
20 min
DMSO
p-nitro-blebbistatin
mRuby2-AHPH (active RhoA) DNA

Figure 2

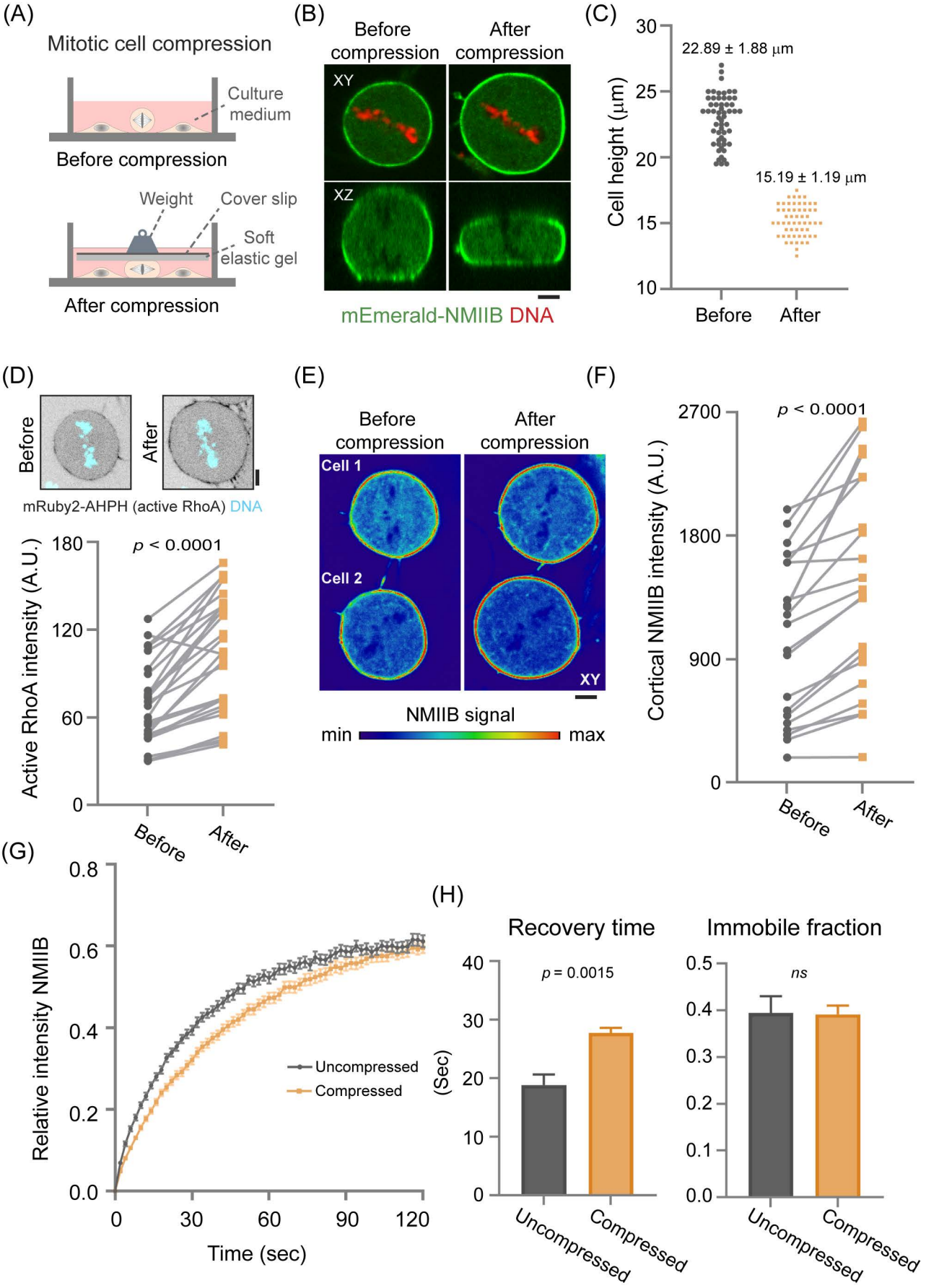
(A)
Mitotic cell compression
Culture medium
Before compression
Weight
Cover slip
Soft elastic gel
After compression
(B)
Before compression
After compression
XY
XZ
mEmerald-NMIIB DNA
(C)
22.89 ± 1.88 μm
15.19 ± 1.19 μm
Cell height (μm)
30
25
20
15
10
Before
After
(D)
Before
After
mRuby2-AHPH (active RhoA) DNA
Active RhoA intensity (A.U.)
p < 0.0001
180
120
60
0
Before
After
(E)
Before compression
After compression
Cell 1
Cell 2
XY
NMIIB signal
min
max
(F)
Cortical NMIIB intensity (A.U.)
p < 0.0001
2700
1800
900
0
Before
After
(G)
Relative intensity NMIIB
0.8
0.6
0.4
0.2
0.0
0
30
60
90
120
Time (sec)
Uncompressed
Compressed
(H)
Recovery time
Immobile fraction
(Sec)
p = 0.0015
ns
40
30
20
10
0
0.5
0.4
0.3
0.2
0.1
0.0
Uncompressed
Compressed
Uncompressed
Compressed

Figure 3

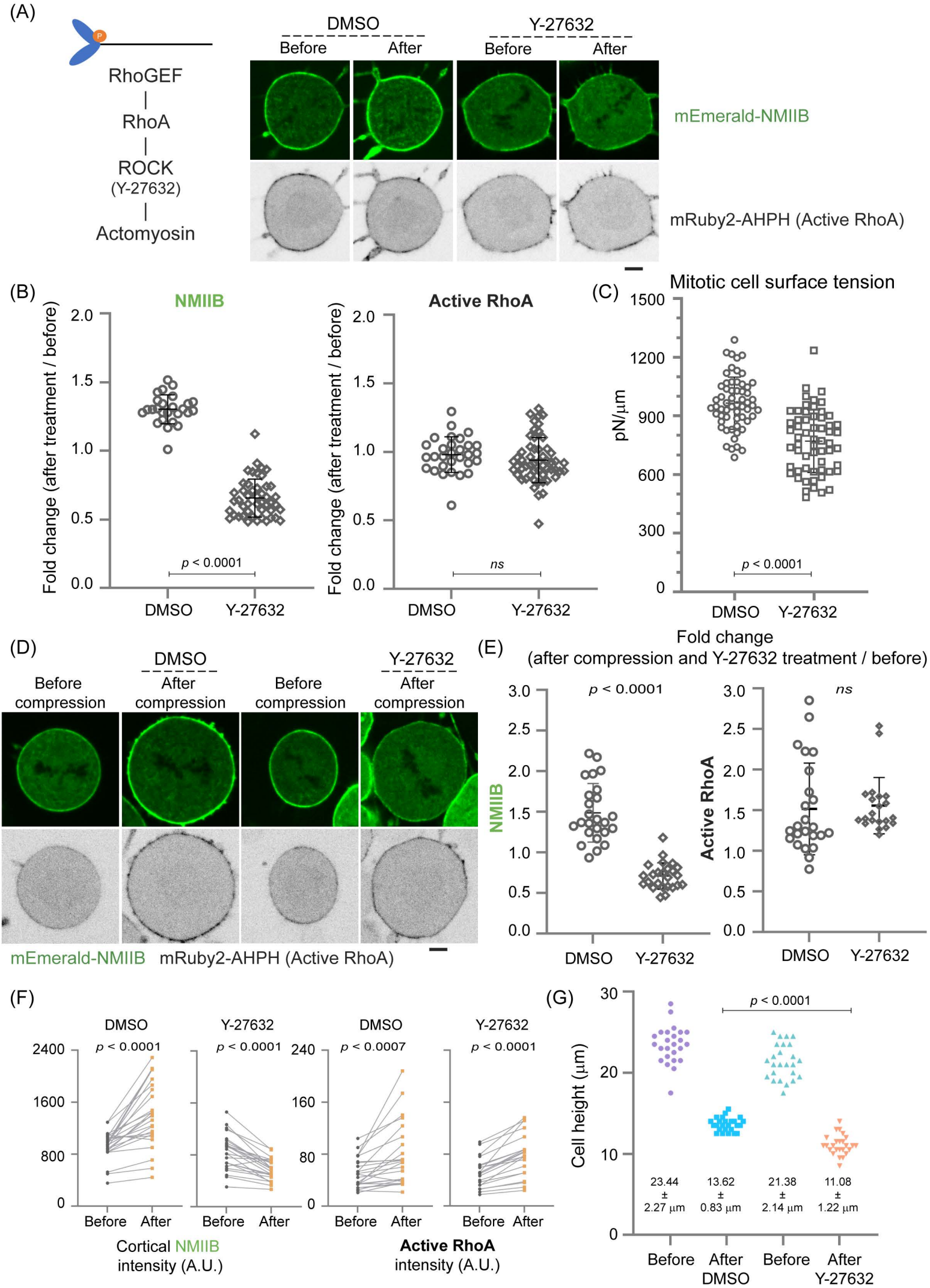
(A)
RhoGEF
RhoA
ROCK
(Y-27632)
Actomyosin
DMSO
Y-27632
Before
After
Before
After
mEmerald-NMIIB
mRuby2-AHPH (Active RhoA)
(B)
NMIIB
Active RhoA
Fold change (after treatment / before)
p < 0.0001
ns
DMSO
Y-27632
(C)
Mitotic cell surface tension
pN/μm
p < 0.0001
DMSO
Y-27632
(D)
DMSO
Y-27632
Before compression
After compression
Before compression
After compression
mEmerald-NMIIB
mRuby2-AHPH (Active RhoA)
(E)
Fold change
(after compression and Y-27632 treatment / before)
NMIIB
Active RhoA
p < 0.0001
ns
DMSO
Y-27632
(F)
DMSO
Y-27632
DMSO
Y-27632
p < 0.0001
p < 0.0001
p < 0.0007
p < 0.0001
Before
After
Cortical NMIIB intensity (A.U.)
Active RhoA intensity (A.U.)
(G)
Cell height (μm)
p < 0.0001
23.44 ± 2.27 μm
13.62 ± 0.83 μm
21.38 ± 2.14 μm
11.08 ± 1.22 μm
Before
After DMSO
Before
After Y-27632

Figure 4

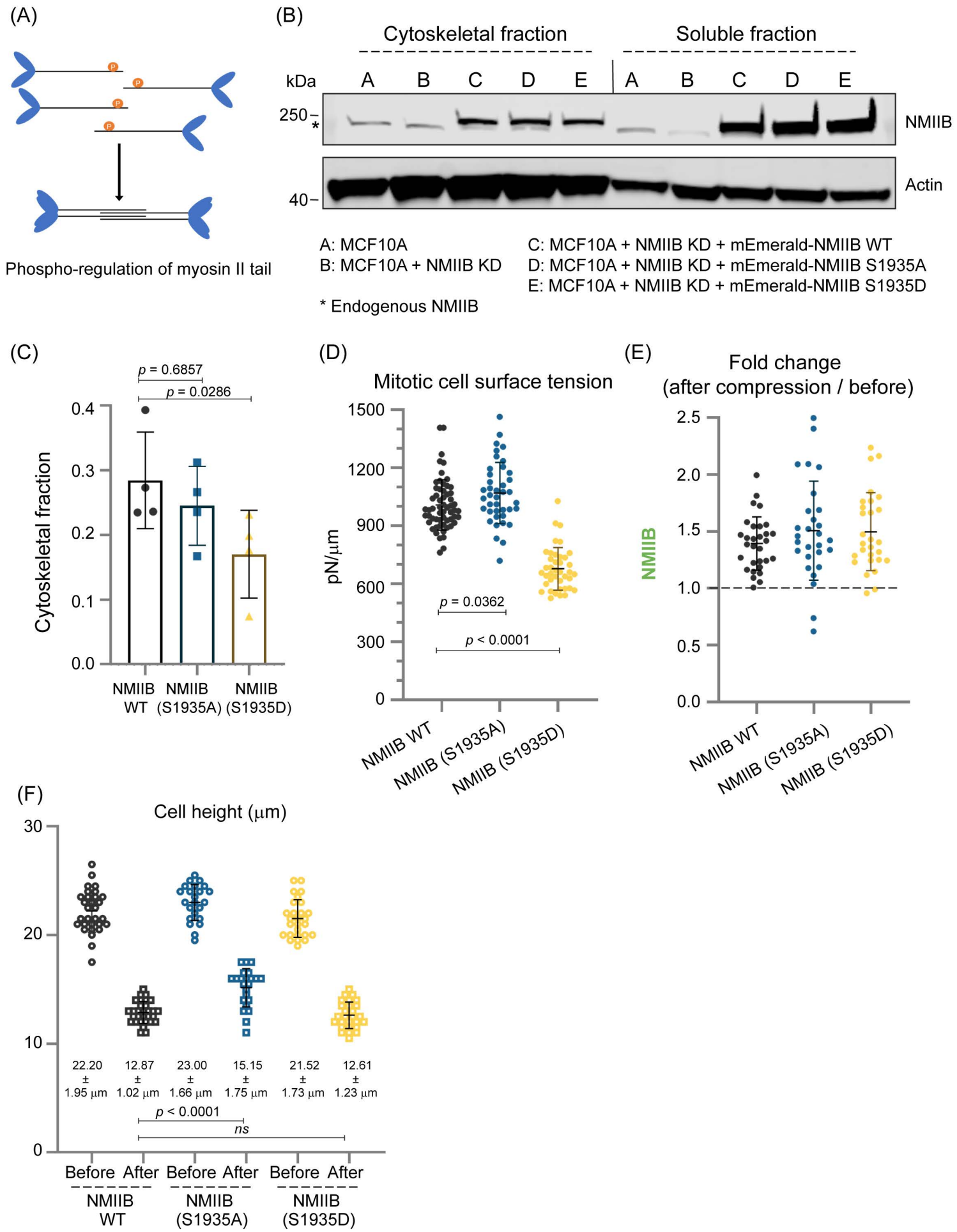
(A)
Phospho-regulation of myosin II tail
(B)
Cytoskeletal fraction
Soluble fraction
kDa
A B C D E A B C D E
250
*
NMIIB
40
Actin
A: MCF10A
B: MCF10A + NMIIB KD
C: MCF10A + NMIIB KD + mEmerald-NMIIB WT
D: MCF10A + NMIIB KD + mEmerald-NMIIB S1935A
E: MCF10A + NMIIB KD + mEmerald-NMIIB S1935D
* Endogenous NMIIB
(C)
p = 0.6857
p = 0.0286
Cytoskeletal fraction
0.4
0.3
0.2
0.1
0.0
NMIIB WT
NMIIB (S1935A)
NMIIB (S1935D)
(D)
Mitotic cell surface tension
pN/μm
1500
1200
900
600
300
0
p = 0.0362
p < 0.0001
NMIIB WT
NMIIB (S1935A)
NMIIB (S1935D)
(E)
Fold change
(after compression / before)
NMIIB
2.5
2.0
1.5
1.0
0.5
0.0
NMIIB WT
NMIIB (S1935A)
NMIIB (S1935D)
(F)
Cell height (μm)
30
20
10
0
22.20 ± 1.95 μm
12.87 ± 1.02 μm
23.00 ± 1.66 μm
15.15 ± 1.75 μm
21.52 ± 1.73 μm
12.61 ± 1.23 μm
p < 0.0001
ns
Before After Before After Before After
NMIIB WT
NMIIB (S1935A)
NMIIB (S1935D)

Figure S1

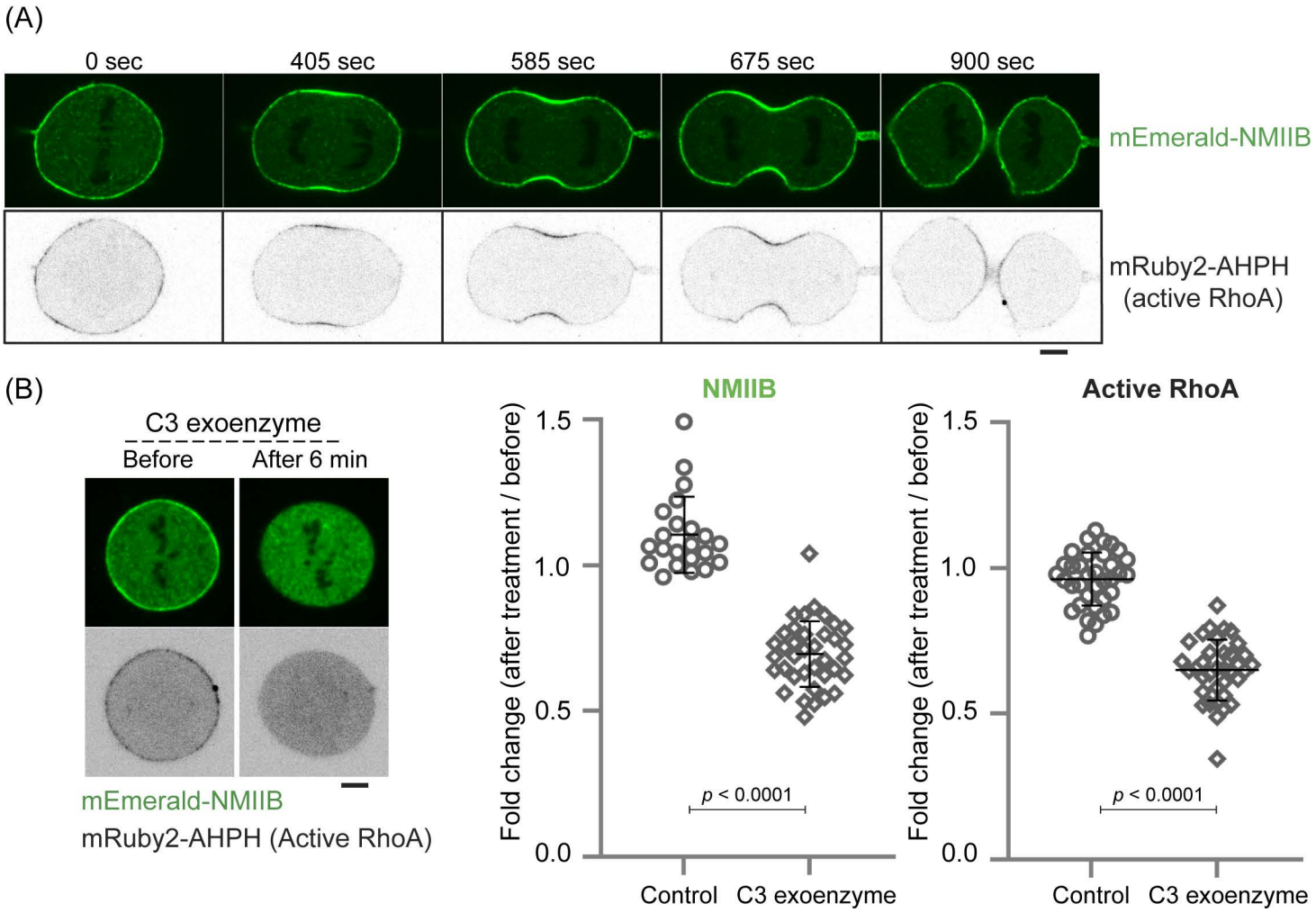
(A)
0 sec
405 sec
585 sec
675 sec
900 sec
mEmerald-NMIIB
mRuby2-AHPH
(active RhoA)
(B)
C3 exoenzyme
Before
After 6 min
mEmerald-NMIIB
mRuby2-AHPH (Active RhoA)
NMIIB
Active RhoA
Fold change (after treatment / before)
1.5
1.0
0.5
0.0
p < 0.0001
Control
C3 exoenzyme

Figure S2

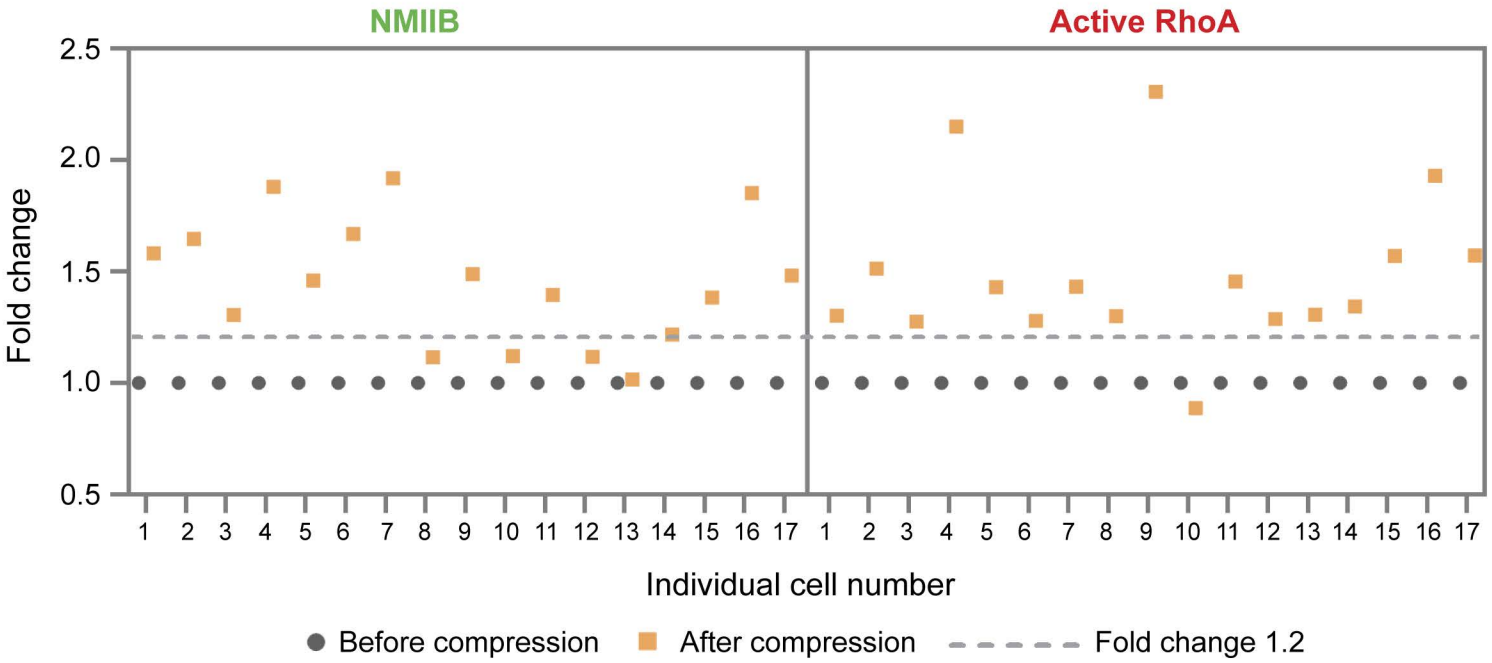

13/17 cells showed at at least 1.2 fold increase of Myosin IIB and active RhoA after compression

Figure S3

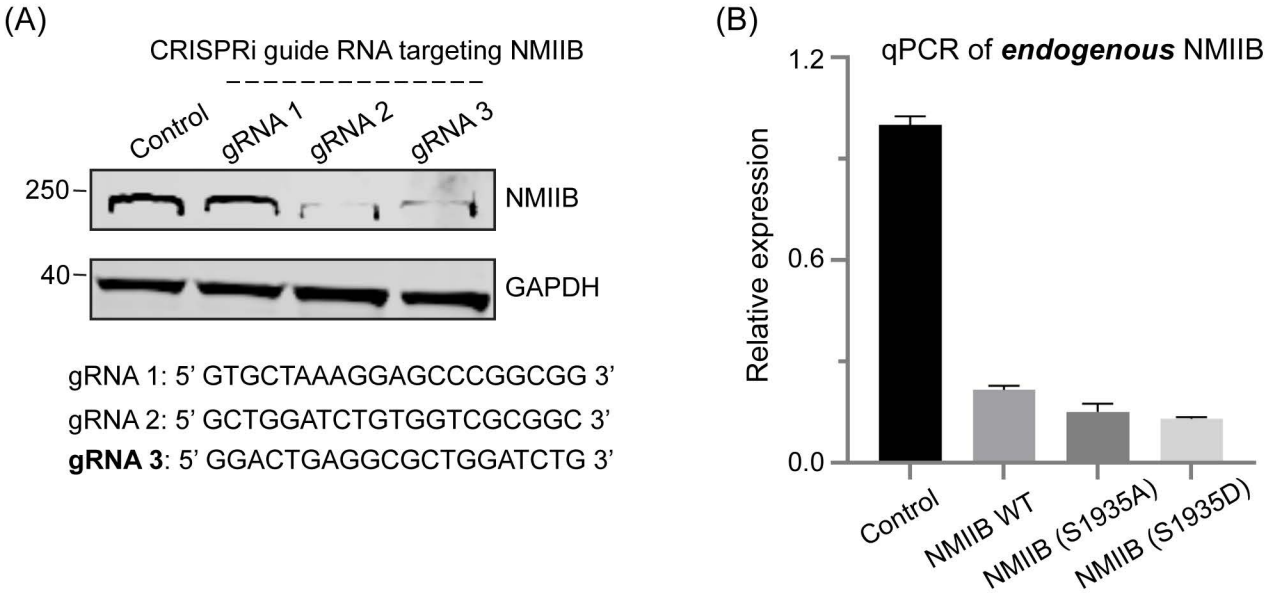
(A)
CRISPRi guide RNA targeting NMIIB
Control
gRNA 1
gRNA 2
gRNA 3
250
NMIIB
40
GAPDH
gRNA 1: 5' GTGCTAAAGGAGCCCGGCGG 3'
gRNA 2: 5' GCTGGATCTGTGGTCGCGGC 3'
gRNA 3: 5' GGACTGAGGCGCTGGATCTG 3'
(B)
qPCR of endogenous NMIIB
Relative expression
1.2
0.6
0.0
Control
NMIIB WT
NMIIB (S1935A)
NMIIB (S1935D)